JACS
JOURNAL OF THE AMERICAN CHEMICAL SOCIETY
pubs.acs.org/JACS
Article

Encapsulation of Gold-Based Anticancer Agents in Protease-Degradable Peptide Nanofilaments Enhances Their Potency

Yaron Marciano, Virginia del Solar, Nazia Nayeem, Dhwanit Dave, Jiye Son, María Contel,* and Rein V. Ulijn*

Cite This: J. Am. Chem. Soc. 2023, 145, 234−246
Read Online

ABSTRACT: We investigated the use of amphiphilic, protease-cleavable peptides as encapsulation moieties for hydrophobic metallodrugs, in order to enhance their bioavailability and consequent activity. Two hydrophobic, gold-containing anticancer agents varying in aromatic ligand distribution (Au(I)-N-heterocyclic carbene compounds **1** and **2**) were investigated. These were encapsulated into amphiphilic decapeptides that form soluble filamentous structures with hydrophobic cores, varying supramolecular packing arrangements and surface charge. Peptide sequence strongly dictates the supramolecular packing within the aromatic core, which in turn dictates drug loading. Anionic peptide filaments can effectively load **1**, and to a lesser extent **2**, while their cationic counterparts could not, collectively demonstrating that loading efficiency is dictated by both aromatic and electrostatic (mis)matching between drug and peptide. Peptide nanofilaments were nontoxic to cancerous and noncancerous cells. By contrast, those loaded with **1** and **2** displayed enhanced cytotoxicity in comparison to **1** and **2** alone, when exposed to Caki-1 and MDA-MB-231 cancerous cell lines, while no cytotoxicity was observed in noncancerous lung fibroblasts, IMR-90. We propose that the enhanced *in vitro* activity results from the enhanced proteolytic activity in the vicinity of the cancer cells, thereby breaking the filaments into drug-bound peptide fragments that are taken up by these cells, resulting in enhanced cytotoxicity toward cancer cells.

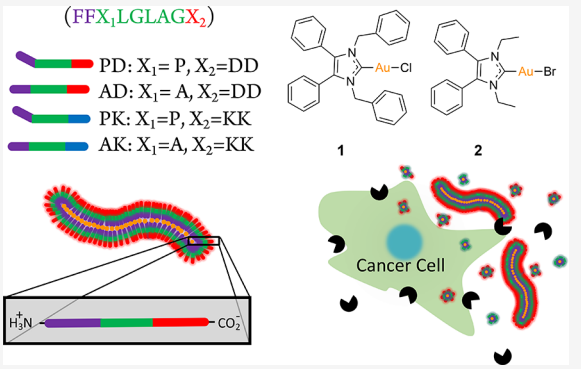

INTRODUCTION

Soft nanomaterials based on polymers and bio(macro)-molecules show significant promise in biomedicine, particularly as delivery systems.[1−3] The physical and chemical properties of nanosized materials can be used to achieve increased circulation times and greater half-lives *in vivo*.[4] Beyond lipid nanoparticles, which have gained much recent attention for their roles in mRNA based COVID-19 vaccines,[5] peptides have emerged as promising nanoscale delivery systems in recent years. Peptide-based materials benefit from chemical versatility, tunable amphiphilicity, reduced barriers to eventual approval by the FDA, and a body of work demonstrating their promise as designable delivery vehicles.[6−8]

Stimuli-responsive peptide-based nanomaterials have been reported to enhance selectivity toward diseased cells and influence drug release kinetics.[9−11] Such stimuli include temperature,[11] pH,[12] and catalytic action of enzymes,[13,14] and can lead to a variety of responses such as particle aggregation, triggered cell-adhesion, particle degradation followed by payload release, or morphology changes of designed nanostructures.[9,11,15,16] The catalytic action of proteases can be exploited as selective biological stimuli to trigger specific responses in peptide-based nanomaterials. Diseased cells, such as cancers, frequently upregulate proteolytic activity, which plays a role in angiogenesis and metastasis.[17] Disease-specific enzymes, including proteases, are therefore particularly promising as stimuli for targeted chemotherapy.[18,19] For example, enzyme-triggered nanofiber formation through supramolecular self-assembly inside cells, or at the cell surface, has been shown to be selectively cytotoxic.[20] Polymeric matrix metalloproteinase (MMP)-responsive materials were first developed as degradable tissue scaffolds.[21,22] Subsequently, there have been various approaches to use MMPs as stimuli for relevant biomedical applications including drug delivery and tissue regeneration.[23−35]

Cancers that are known to overexpress proteases include triple negative breast cancer (TNBC) and renal cancer (MMP-2, MMP-9),[30,36,37] which are both difficult to target. TNBC is aggressive and highly metastatic, and a main factor leading to TNBC morbidity is its "molecular heterogeneity", described as a "lack of recurrent oncogenic driver alterations".[38] There are

Received: September 14, 2022
Published: December 21, 2022

https://doi.org/10.1021/jacs.2c09820
J. Am. Chem. Soc. 2023, 145, 234−246

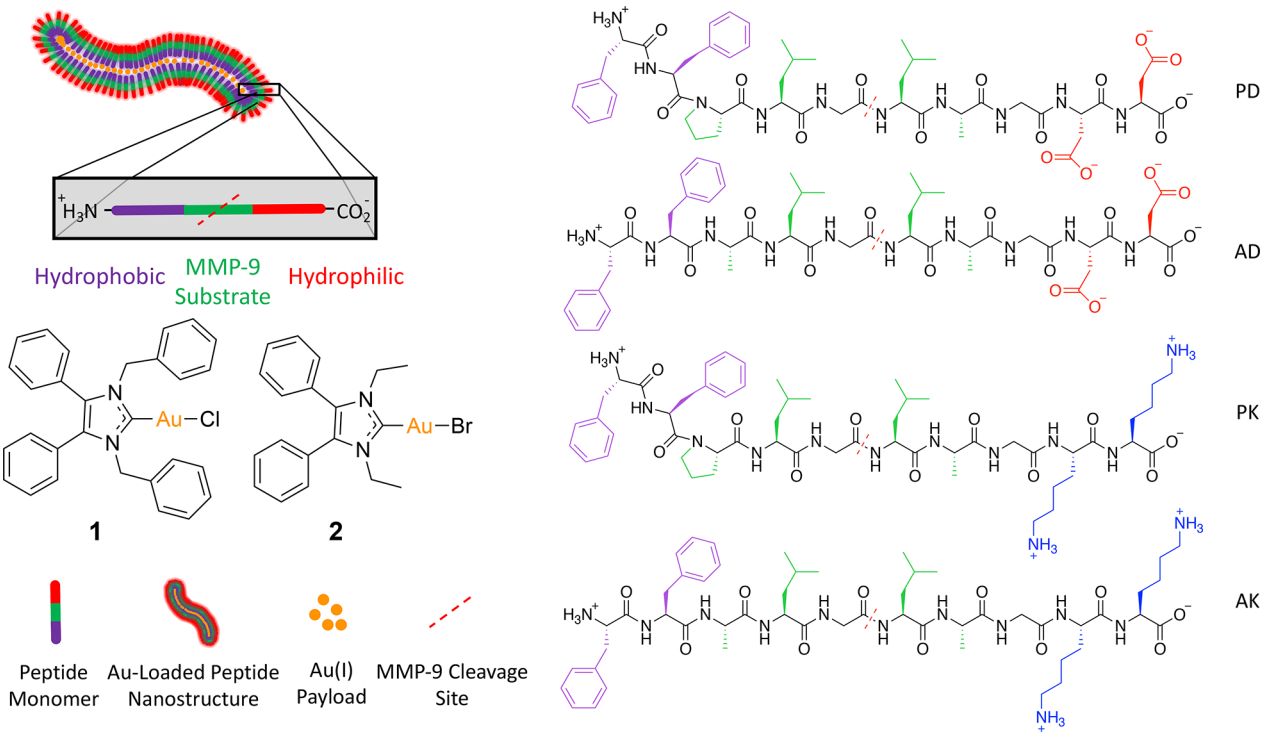

Figure 1. Cartoon of drug-loaded self-assembling peptides and chemical structures of peptides and drugs investigated in this work.

two recently approved targeted therapies for TNBC in the clinic, an antibody–drug conjugate[39,40] and a PARP inhibitor,[41] but chemotherapy is still the standard treatment. Renal cancer is one of the most common types of cancers for both men and women, with clear cell renal cell carcinoma (ccRCC) being the most prevalent (70%).[42,43] Current treatment options include targeted therapies such as mTOR and HIF2a inhibitors, and immunotherapy, though both have low survival rates.[44] Chemotherapies (5-FU and capecitabine) are also used, though only to modest responses and survival rates.[45] The development of new drugs and new ways of delivering them to the target site is desired and protease-responsive strategies may hold promise for TNBC and renal cancer.

Since the discovery and subsequent FDA approval of the Pt(II) compound, cisplatin, for the treatment of various cancers, there has been much interest in metal-based compounds in the biomedical field as both therapeutic and diagnostic agents. Cisplatin, either alone or in combination therapy, is currently one of the most commonly used chemotherapeutic agents in the clinic.[46] However, cisplatin is also associated with drawbacks. These include acquired resistance in cancer cells after treatment, an optimal spectrum of activity that is limited to specific cancers, a lack of selectivity, and consequent severe side effects that can limit its dosage in the clinic.[47] In recent years, a number of alternative metal-based compounds that are highly effective, less toxic, and selective in cisplatin-resistant cancers have been described,[48−51] including prodrugs that are designed to selectively activate at the target site.[52] There are examples of Ru(II), Ru(III), and Au(I) compounds currently in clinical trials.[53−56]

Au(I) compounds have a different mode of action compared to Pt(II)-based derivatives. While Pt(II) compounds, such as cisplatin, generally act through their interactions with DNA, gold compounds inhibit specific enzymes. For example, Au(I) has a strong binding affinity to sulfides, which makes enzymes such as thioredoxin reductase (TrxR), glutathione reductase, and cysteine proteases (all of which are overexpressed in cancer cells) potential targets for gold chemotherapeutics.[57] Moreover, Au(I) compounds are becoming attractive not only due to their antitumor effects that involve apoptosis, antimigratory and antiangiogenic properties, but also because they may produce immunogenic cell death.[58] Au(I)-*N*-heterocyclic carbene (NHC) complexes, specifically, have shown exceptional stability, and reduced toxicity in physiological conditions, when compared to gold compounds containing other ligands. Au(I) compounds containing NHCs have displayed promising anticancer activity including high *in vivo* efficacy in TNBC and renal cancers.[57,59−63] While there are many reports on the encapsulation of platinum and ruthenium compounds with potential anticancer properties, encapsulation of gold compounds has not been thoroughly explored.[64]

Given developments in gold-based chemotherapy, and the promise of proteolytically degradable, peptide-based materials as drug delivery vehicles, we decided to combine these concepts and develop targeted delivery of hydrophobic gold-based chemotherapeutics using designed peptide nanostructures. We hypothesize that hydrophobic metal-based payloads can be loaded into the core of amphiphilic self-assembling peptide nanofilaments, and through peptide design we will determine the effect of charge and peptide packing on nanostructure formation, loading efficiency, and cytotoxicity, which is expected to be regulated by enhanced proteolytic activity surrounding cancer cells. We report here on the encapsulation of two cytotoxic Au(I)-*N*-heterocyclic carbene compounds in selected amphiphilic peptide nanostructures (Figure 1). The anticancer properties in TNBC and renal

https://doi.org/10.1021/jacs.2c09820
J. Am. Chem. Soc. 2023, 145, 234−246

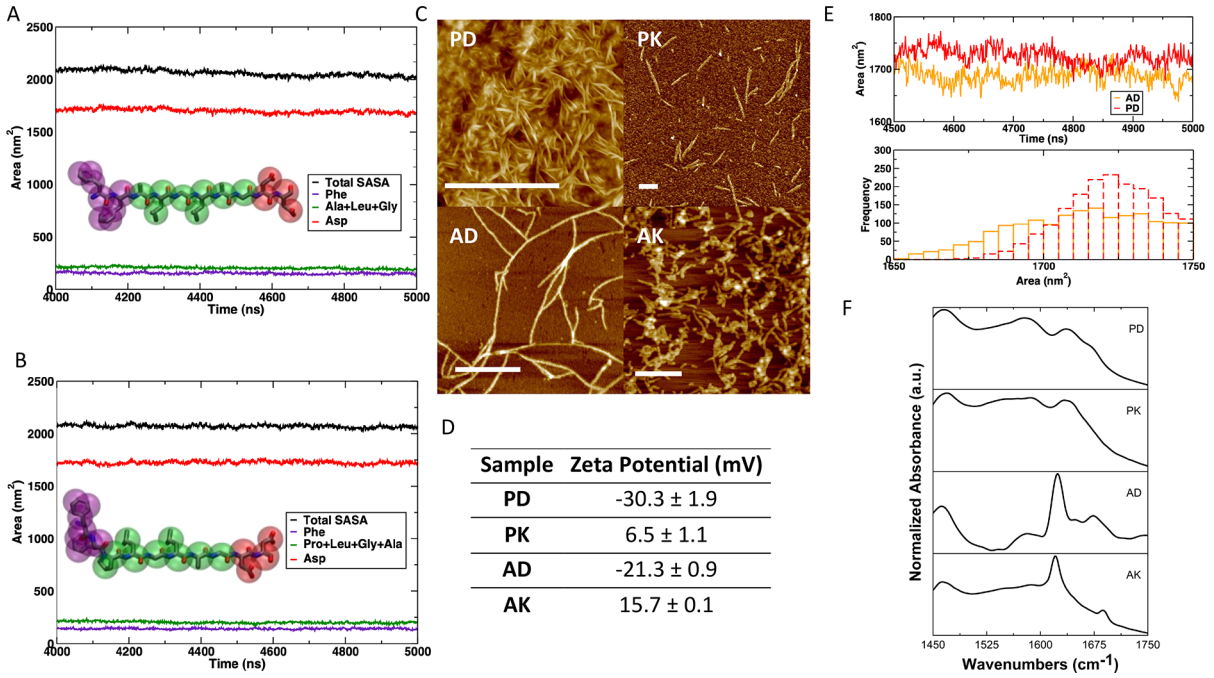

Figure 2. Characterization of self-assembly behavior of peptide nanostructures (1 mM **PD**, **PK**, **AD**, **AK**). Coarse-grained MD simulations (solvent accessible surface areas, SASAs) of (A) **AD**, (B) **PD**. (C) AFM images of self-assembled peptide nanostructures (scale bar 500 nm). (D) Zeta potential analysis of peptide nanostructures. (E) SASAs of terminal DD residues in **PD**, **AD** showing differential exposure of charged residues. (F) FT-IR of peptides in the Amide I region.

cancer cell lines are explored and compared with noncancerous lung fibroblasts.

The peptide designs explored build on our previous work. We reported that doxorubicin could be loaded into MMP-9 responsive peptides, and these underwent MMP-9 triggered micelle-to-fiber transitions, leading to localized drug release and tumor growth inhibition *in vivo*.[16,30] These peptides were comprised of three segments, namely, diphenylalanine as a self-assembling motif,[65,66] an MMP-9 cleavable substrate, and a hydrophilic, charged segment. The MMP-9 sensitive sequence was based on data from the MEROPS database,[67] suggesting that MMP-9 cleavage is preferentially observed between Gly and Leu (G↓L) residues. We demonstrated that net charge and packing order/disorder could modulate enzyme engagement and hydrolysis kinetics, which could be tuned over a significant range.[15] Four of our previously studied peptides[15] were chosen to load with hydrophobic gold compounds (Figure 1). We sought to investigate the effect of net charge, and β-sheet packing on drug loading, and we therefore chose the following sequences: **PD** (FFPLGLAGDD), **PK** (FFPLGLAGKK), **AD** (FFALGLAGDD), and **AK** (FFALGLAGKK). The Pro residue introduces a kink into the backbone of **PD** and **PK** (Figure 1), which affects the β-sheet formation and assembly, and we sought to determine whether replacement with an Ala (**AD**, **AK**) residue would affect drug loading. These peptides assemble into 1D nanostructures, and at concentrations studied here (1 mM), they appear as clear solutions. One potential advantage of these soluble elongated, filamentous nanomaterials over spherical nanoparticles is an increased circulation time *in vivo*, which has been reported to be up to ten times longer compared to spherical particles.[68]

The structures of the two hydrophobic Au(I)-based drugs selected for this study (neutral compounds containing *N*-heterocyclic carbenes derived from 4,5-diarylimidazoles and halide) are shown in Figure 1. They have shown anticancer efficacy previously and are expected to interact favorably with the aromatic diphenylalanine cores of the supramolecular peptide nanostructures. The anticancer compound NHC-AuCl (**1**) (1,3-dibenzyl-4,5-diphenylimidazol-2-ylidene)gold(I) chloride, described by Tacke and co-workers,[69] has shown promising cytotoxic activity against a wide range of human cancer cell lines from the NCI 60-cell-line panel.[61] Compound **1** has also shown tumor growth inhibition *in vivo* for a human clear cell renal carcinoma Caki-1 xenograft mice model.[61] Compound **2** (1,3-diethyl-4,5-diphenylimidazol-2-ylidene)-gold(I) bromide, first described by Gust and co-workers,[70] was found to be cytotoxic in breast and colon cancer cell lines (MDA-MB-231, MCF-7, and HT-29, respectively) in the low micromolar range.

RESULTS AND DISCUSSION

Structure and Encapsulation of Gold Compounds in Charged Amphiphilic Peptides. The four peptides selected, **PD**, **PK**, **AD**, and **AK**, were synthesized using Fmoc-based solid phase peptide synthesis (SPPS), and purified as previously reported, with particular attention to removal of any residual trifluoroacetic acid (TFA).[15] To generate insights into the self-assembly of these four peptides we used coarse grained molecular dynamics (MD) simulations, AFM, zeta potential, and FT-IR (Figure 2). Coarse Grained MD simulations indicate that the self-assembly of these peptides is primarily driven by rapid sequestration of the FF (represented by purple beads) and XLGLAG (green beads) into the core of the aggregates (Figure S1A–D). Solvent accessible-surface areas (SASAs) of all four peptides show that upon assembly, the hydrophobic (FF) and MMP-9 substrate (XLGLAG) segments are buried within the core, while the charged segments (diaspartic acid, DD for **PD**, **AD**, and dilysine, KK for **PK**, **AK**) are exposed on the exterior and have

https://doi.org/10.1021/jacs.2c09820
J. Am. Chem. Soc. 2023, 145, 234–246

greater interactions with the solvent (Figure 2A,B, Figure S1G−K). Overall peptide aggregation propensity trends show a higher assembly propensity for the KK terminating peptides (**AK** and **PK**) due to favorable complementary electrostatics with the C-terminus (Figure S1E,F). The peptides assemble into nanofilaments (Figure S2) and can be observed experimentally using AFM (Figure 2C, S3). The aspartic acid (D), and lysine (K) containing peptides have a −2, and +2 net charge (7.4 pH), respectively, and this is reflected in the zeta-potential of the self-assembled structures (Figure 2D, S4). MD simulations show the increased SASA of the D-beads in **PD**, compared to **AD**, providing an explanation for the observed differences in zeta-potential values (−30.3 ± 1.9 mV for **PD**, −21.3 ± 0.9 mV for **AD**) (Figure 2E). We can see a similar effect for the Lys containing peptides (Figure S1L). Observing the Amide I region in the FT-IR spectra, we can see the effects of Pro residue on the secondary structure, with both **PD**, **PK** containing disordered hydrogen bonds (1640−1650 cm^{-1}), while **AD**, **AK** contain sharp parallel β-sheet peaks in the 1620 cm^{-1} range (Figure 2F). We verified the stability of these peptides and observed low levels of hydrolysis in phosphate buffer at physiological conditions, up to 72 h (Figure S5).

To load gold compounds **1** and **2** into the peptide nanostructures, we developed the protocol shown in Figure S6, which involves peptide self-assembly to encapsulate gold compounds, followed by free gold precipitation, and subsequent centrifugation to separate free gold compounds **1** and **2** from encapsulated material and using atomic absorption spectroscopy (AAS) for gold quantification. To validate this protocol, dissolution of free **1** and **2** was attempted in phosphate buffer and minimal gold content was observed using AAS (Table S1). Due to the sparingly soluble nature of **1** and **2** (<1.5%), any gold that remains present in the aqueous supernatant, in amounts greater than what was observed in buffer solution, is presumed to be associated with the supramolecular peptide nanostructure through encapsulation (Figure 1).

The critical aggregation concentrations of the four selected MMP-responsive peptides were previously found to be below 1 mM;[15] therefore, 1 mM peptide was used along with varying micromolar concentrations of the gold compounds. The encapsulation efficiency (EE) of gold compounds into the peptide assemblies at different gold concentrations (up to 500 μM) is shown in Figure 3. Encapsulation efficiency, loading capacity (LC) and weight percent (wt %) were calculated using the equations shown in Figure S7 and shown in Table S2A,B. The critical aggregation concentrations (CAC)s of the two anionic peptides in the presence of gold (compound **1**) were evaluated using **PD**+**1** 10 μM and **AD**+**1** 10 μM (where the μM concentration refers to the stock gold concentration used in sample preparation). The measured CACs observed for the loaded peptides (Figure S8) is consistent with the unloaded peptides (where **PD** < **AD**).[15] Therefore, the presence of the gold compounds does not significantly impact on the CAC of these peptides.

Comparing the encapsulation efficiencies of anionic and cationic peptides, minimal gold is detected in both cationic peptides with both compounds **1** and **2**. We propose that positively charged lysine residues of **PK** and **AK** (pH 7.4) cause electrostatic repulsions with the cationic gold center, explaining the observed reduced drug loading. In anionic peptides, comparing **1** and **2**, we can see the increased loading

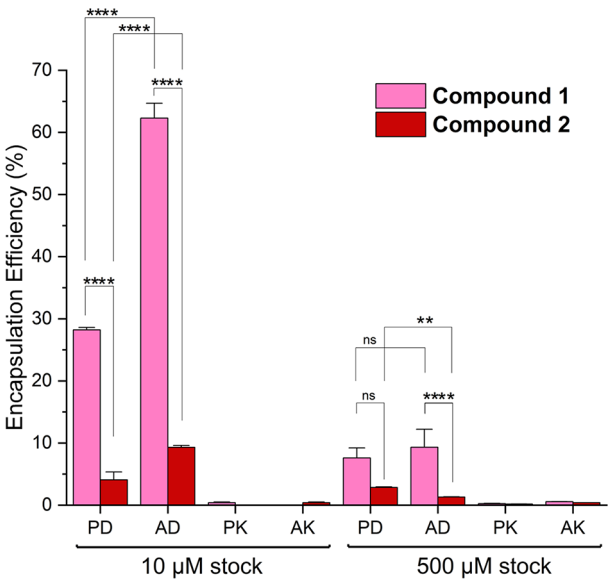

Figure 3. Encapsulation efficiency (%) of peptides (**PD**, **AD**, **PK**, **AK**) (1 mM) with two gold compounds (**1**, **2**), at two stock concentrations (10, 500 μM). Gold quantified using AAS at 242.8 nm. (* represents $P < 0.05$, ** represents $P < 0.01$, *** represents $P < 0.001$, **** represents $P < 0.0001$).

of **1** relative to **2** (>6 fold for **PD**, **AD**, using 10 μM stock, >2 fold for PD, >7 fold for AD, using 500 μM stock). This can be attributed to the increased hydrophobicity of **1**, due to the two additional benzene rings on the NHC ligand that are expected to interact favorably with the FF peptide motif, compared to the ethyl groups on the NHC ligand of **2**. We can also see that the replacement of Pro with Ala (**PD** → **AD**) leads to increased drug loading, most notably for **1**. This is likely due to increased packing of the supramolecular structure, and the presence of β-sheet motifs[15] which provides a hydrophobic face that can act as a binding domain for the gold compounds. Therefore, peptide design clearly affects drug loading capacity.

Based on the observed drug loading values, we moved forward with two anionic peptides, **PD** and **AD**. These peptides differ by the replacement of Pro with Ala, and a consequent up to 2-fold difference in loading capacity. In terms of MMP-responsiveness, we note that in direct comparison using preactivated MMP-9 showed that the anionic peptide structures had reduced responsiveness to MMP-9 compared to the cationic counterparts in an aqueous buffer system due to electrostatic mismatching between the enzyme and nanostructure.[15] Anionic peptide nanostructures were previously found to be effective in both *in vitro* and *in vivo* experiments.[30]

Characterization of Loaded Peptide Nanostructures. The drug-loaded peptide nanostructures were characterized using zeta potential analysis, AFM, TEM, and FT-IR. The zeta potential values of the drug-loaded peptides (Figure 4A, Figure S9) revealed the expected negative charges, due to the presence of two charged Asp residues on the C-terminus, though lower for the drug-loaded peptide filaments, relative to free peptide. The observed increase in surface charge supports that gold compounds are not bound to the exterior of the assembled structure but encapsulated within the core, and results in enhanced exposure of D residues in particular for **AD**, suggesting some disruption of peptide packing. Fourier Transform Infrared Spectroscopy (FT-IR) was used to assess whether the peptide assembly is impacted upon the presence

https://doi.org/10.1021/jacs.2c09820
J. Am. Chem. Soc. 2023, 145, 234−246

A

Sample	Zeta Potential (mV)
PD+1 10 μM	-33.0 ± 1.0
PD+2 10 μM	-46.4 ± 1.7
AD+1 10 μM	-35.5 ± 1.7
AD+2 10 μM	-37.7 ± 1.4

B

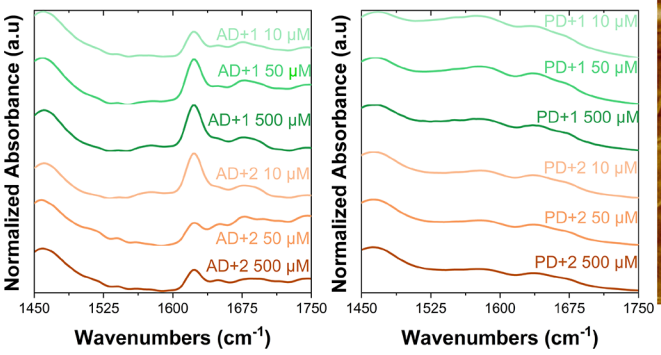

C

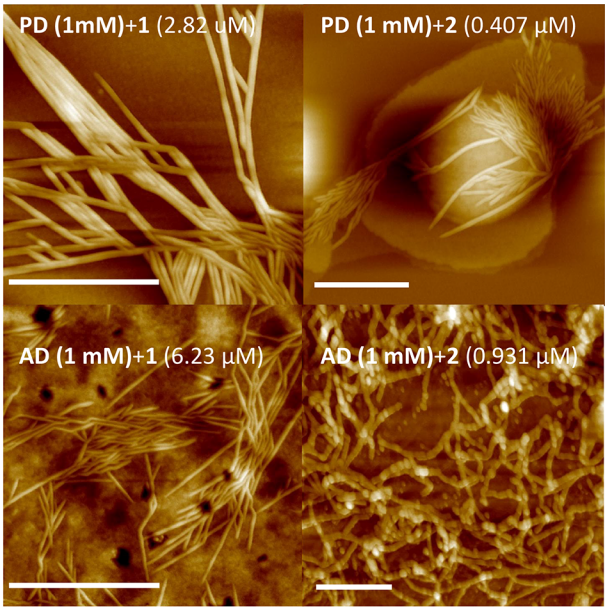

Figure 4. (A–C) Characterization of gold-loaded peptide nanostructures. (A) Zeta potential analysis of peptides (**PD**, **AD**) loaded with **1**, **2**. (B) FT-IR of the drug-loaded peptides in the Amide I region. (C) AFM images of self-assembled (drug-loaded) peptide nanostructures. (1 mM peptide, scale bar 500 nm).

of gold compounds (Figure 4B). The Amide I region was investigated to detect any changes to the backbone H-bonding patterns of these assemblies. For **PD**, no changes were observed, even with the highest concentrations of either of the gold compounds, indicating they do not disrupt the assembly. For **AD**, a sharp peak at 1620 cm^{-1} was observed in the presence of the drugs, although there is an emergence of a broad peak at 1650 cm^{-1} when loaded with **2**, indicating disordered hydrogen bonds, and some disruption of the assembly. This emphasizes that chemical properties of the metallodrug's ligands can be matched with peptide design to maximize its interactions with the hydrophobic pocket of the assembly. AFM imaging of the drug-loaded peptides shows filaments, confirming that the presence of gold compounds does not disrupt or prevent peptide assembly (Figure 4C). Certain combinations of peptide and gold lead to the formation of thicker, longer, and increasingly bundled fibers. Specifically, we observed a significant amount of bundling of fibers for **PD+1**, and less for **AD+1**, likely due to the difference in loading observed. Similarly, the bundling is less defined for the peptides containing **2**, and in the case of **AD+2**, no bundling of fibers is observed. We note that observed filament bundling may be in part resulting from samples drying prior to imaging. Similarly, TEM images of **PD** loaded with **1** appear more bundled, compared to **AD** loaded with **1**. Additional AFM images, and TEM images of **AD**, **PD** loaded with **1**, the most efficiently loaded drug, can be found in Figures S10–S11.

MMP-9 Expression and Inhibition. Because these peptides were designed to be cleavable by MMP-9, we set out to determine if the drug-loaded peptides can selectively release their payload in near cells that overexpress MMP-9. We chose cancerous cell lines known to overexpress MMP-9,[30,36,71] and for which the selected gold compounds were reported to have relevant effects,[69,70] specifically, MDA-MB-231 (TNBC) and Caki-1 (ccRCC). The noncancerous control cell line selected was IMR-90 (lung fibroblasts), which has been reported to not overexpress MMP-9.[72] Using an ELISA kit, MMP-9 expression of the cell lines was quantified, both in cells and in media (Figure S12A–C). We expected to observe higher enzyme concentrations in media, as MMP-9 is secreted from the cell membrane.[73] MMP-9 was only detected in MDA-MB-231, and as expected, a greater amount (6-fold) was detected in media compared to in the cells. MMP-9 expression in renal cell carcinoma tissue has been reported previously,[71] but the concentrations were below detection limit in our assay. Enzyme expression may not correlate to activity due to the presence of tissue inhibitor of metalloproteinases (TIMPs).[71] We therefore also performed a gelatin zymography assay to qualitatively detect levels of active MMP-9 in the three cell lines of interest (Figure S13A–D). As MMP-9 is a gelatinase, we were able to detect levels of active enzyme by observing the density of the band in the gel. Interestingly, we found that there is more active MMP-9 in Caki-1 cells than in MDA-MB-231. As expected, we observed no detectable MMP-9 activity in the noncancerous (IMR-90) cells. We observed significant MMP-2 activity in IMR-90 cells, but not in the two cancerous cell lines. Increased MMP-2 activity in healthy cells has been reported previously.[74,75] To determine whether gold compounds inhibited MMP-9 expression, MDA-MB-231 cancer cells were treated with **1** and **2**. Quantification of MMP-9 (ELISA) confirmed that gold compounds do not significantly inhibit MMP-9 expression (Figure S14).

MMP-9 Kinetics and Payload Release. MMP-9 cleavage of peptides was analyzed using LC-MS, and we observed a significant reduction in hydrolysis in the enzymatic degradation of gold-loaded peptide nanostructures (Figure S15). As in the unloaded peptide filaments, **PD** is cleaved (although incompletely) while **AD** is not. The reason is that highly organized fibers, in our case, **AD**, are less susceptible to enzymatic degradation. MMP-9 has been shown to hydrolyze type I fibril collagen,[76] and the Pro residue in **PD** enhances cleavage through closer semblance with collagen.[77] **PD** is

https://doi.org/10.1021/jacs.2c09820
J. Am. Chem. Soc. 2023, 145, 234–246

designed to be cleaved between Gly and Leu residues, with FFPLG being the cleavage product. For **PD** loaded with **1**, we observe a decrease (~50% cleavage), compared to ~80% for unloaded **PD**. **PD** loaded with **2** shows even lower hydrolysis (~30%). We propose that the incorporation of gold and subsequent change in morphology may prevent optimal enzyme engagement with the peptide backbone leading to reduced hydrolysis. The AFM images of **PD**, **AD** loaded with **1** and **2** and incubated with MMP-9 for 72 h are shown in Figure S17. As expected, we observed formation of random aggregates upon cleavage for loaded and unloaded **PD**, and retention of nanofilaments for loaded and unloaded **AD**. We observe different morphologies among the loaded **AD** samples, likely due to interactions with the drugs in the core of the assemblies.

When quantifying released gold during cleavage experiments, a number of observations could be made (Figure S16). Gold release was measured while incubating peptides **PD** and **AD** containing gold compounds **1** and **2** with MMP-9 for 72 h and compared to controls not incubated with the enzyme. During incubation, peptide controls release 50−95% gold over 72 h. For both drugs, **AD** shows similar payload release in the presence and absence of MMP-9 (Figure S16B), which is expected due to the lack of peptide hydrolysis (Figure S15). Surprisingly, when **PD** is incubated with MMP-9, we observed a decrease in gold release (<50% payload release after 72 h) compared to **AD** (dashed blue/purple traces, Figure S16). These results suggest that the payload remains associated with the enzymatic product of **PD**, FFPLG, which loses its propensity to form filaments but remains aggregated.

Activity on Cancerous Cells. Having established that metallodrugs can be loaded into nanofilaments, and that in particular **PD** filaments are MMP-9 cleavable, we investigated the cytotoxic effect of the drug-loaded peptides on cancerous and noncancerous cell lines (Figure 5) compared to the free drugs. To observe differences in activity between free gold compounds and gold-loaded peptides, we decided to measure cell viability at a single concentration of gold compound (2 μM of **1**, 1 μM for **2**, both free and encapsulated) after 72 h. We expected to see decreased cell viability in the cancerous cells, as we observed MMP-9 activity,[78] and in particular for **PD**, leading to the cleavage and subsequent breakdown of fibers and facilitated uptake of the cytotoxic gold compounds (which, as discussed, likely remain associated with postcleavage peptide fragments). Both **AD** and **PD** peptide filaments alone were found to be nontoxic to the cell lines at a concentration of 1 mM. A decrease in cell viability for both drug-loaded peptides was observed with respect to the peptides or the gold compounds alone for the cancerous cells that express MMP-9 (MDA-MB-231 and Caki-1) (Figure 5). Increased selectivity toward cancerous cells was observed, which is markedly higher for Caki-1 renal cell lines for **1** and **2**, and also for MDA-MB-231 (TNBC) for compound **1**. This cell viability decrease is more pronounced for encapsulated compound **1** than for compound **2** for the TNBC cell line. The increased activity observed for drug-loaded peptides compared to the free drug indicates that lower drug doses are required to achieve cell death. The similarity between the activity of gold-loaded **AD** and **PD** was not expected based on the difference *in vitro* MMP-9 cleavage. We note the possibility that **AD** and **PD** peptide cleavage by other nonspecific secreted proteases that are upregulated by highly active cancer cells[17] may contribute to localized action of peptide carriers, as investigated further

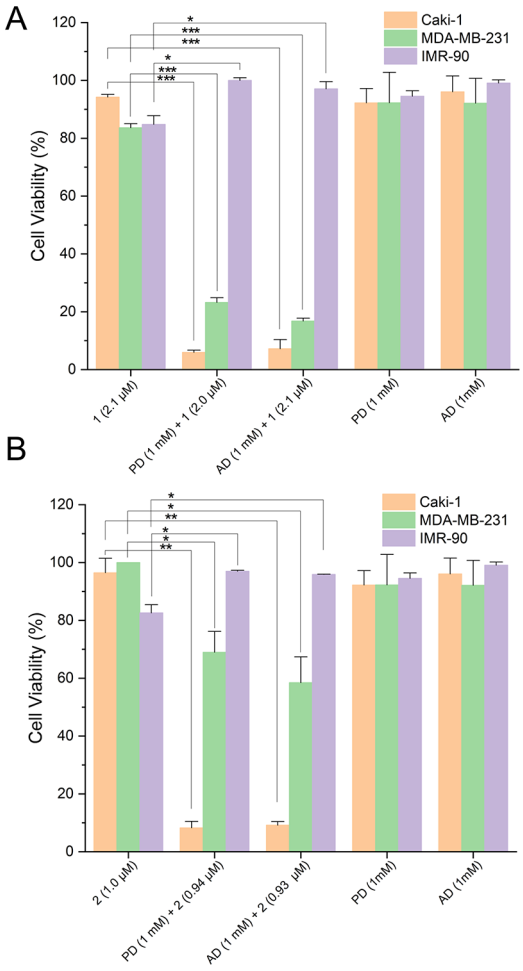

Figure 5. (A,B) Viability of gold anticancer agents, gold-loaded peptide nanofilaments (**PD+1**, **PD+2**, **AD+1**, **AD+2**), and peptides (**PD**, **AD**) in three human cell lines. Caki-1 (renal cancer), MDA-MB-231 (Triple Negative Breast Cancer), and IMR-90 (lung fibroblasts) incubated with drug-loaded peptide for 72 h. (A) Compound **1**, (B) Compound **2**. (* represents $P < 0.05$, ** represents $P < 0.01$, *** represents $P < 0.001$).

below. Additionally, observed enzyme kinetics and release *in vitro* may not accurately reflect the cell culture conditions.

We interpret the observed difference in activity between healthy cells and cancer cell lines as resulting from the overall differences in proteolytic activity around these cells, which facilitates breakdown of peptide filaments. In order to support this hypothesis, we carried out further stability studies of peptides **PD** and **AD**, and their hydrolysis peptide filaments by simulating the increased proteolytic activity surrounding cancer cells. The media used for the cell viability experiments was incubated with cells for 24 h before centrifugation and removal of cells. Peptide filaments were then incubated with the media at 37 °C in order to better understand the general proteolytic activity *in vitro*. MDA-MB-231 and IMR-90 cell lines were incubated with DMEM (Dulbecco's Modified Eagle Medium), and Caki-1 cells were incubated with RPMI (Roswell Park Memorial Institute Medium). The stability of the peptide filaments was also tested in standard media as a control (Figure S18). For both peptides in both media, we can see significant peptide degradation after 24 h, and this degradation is enhanced with media incubated with different cell lines. This is indicative of the increased general proteolytic

https://doi.org/10.1021/jacs.2c09820
J. Am. Chem. Soc. 2023, 145, 234−246

activity of cancerous cells. The IMR-90 fibroblasts also show substantial hydrolysis, although less than MDA-MD-231. When comparing the two media, it is clear that peptides are more stable in RPMI media relative to DMEM. This is likely due to the presence of several inorganic salts in DMEM that may assist in cleaving amide bonds. Peptide cleavage patterns were explored and showed the increased presence of phenylalanine, di- and tripeptides forming in the simulated proteolytic environment of cancerous cells (Figure S19). This suggests increased activity of aminopeptidases that may be further hydrolyzing the parent peptides or MMP-9 hydrolysis product (for **PD**).[79−83] We observed that both free and peptide encapsulated drugs are effectively taken up by cells (Figure S20) and propose that the nanofilaments are broken up into drug-bound fragments that give rise to different interactions with the cancerous cells. In order to probe differences when comparing free drug and peptide-encapsulated drug, cell death experiments at 24 and 72 h showed that **PD+1** exerts apoptosis more effectively (2-fold) than free compound **1** (Figure S21) in Caki-1 cells. These results therefore further confirm the remarkable efficacy enhancement of the drug when formulated with biodegradable peptide filaments. Gold(I) N-heterocyclic carbene compounds of the type [Au(NHC)Cl] are known to quickly exchange the chloro ligand and bind to S- and Se-containing enzyme active sites (e.g., cysteine and selenocysteine) in biological media.[84,85] This usually causes inhibition of these enzymes provoking cell death, but the coordination is nonselective and the compounds may also be deactivated this way.[85] The loss of Cl and subsequent coordination of the resulting cation $[Au(I)\text{-}NHC]^+$ to peptide fragments may generate new bioconjugates that may be more cytotoxic and selective than [Au(NHC)Cl] precursors once internalized by the cells, as has been reported for gold and other metals.[86−88]

We show that peptide filaments can be effectively loaded with drugs, that drug-loaded peptide filaments are proteolytically degraded, and that drugs likely remain associated with peptide fragments, resulting in enhanced efficacy. Future work includes the elucidation of the mechanism of action, with a particular focus on the role and binding of postcleavage peptide fragments facilitating the action of these gold compounds.

CONCLUSION

In conclusion, we have developed peptide nanofilaments that enable encapsulation of gold-based anticancer agents. We found that peptide sequence dictates the drug loading, with aromatic drug conjugates achieving a higher loading in the aromatic core of the peptides and does not prevent self-assembly. Peptide design dictates packing, which impacts on the drug loading, as the swapping of one amino acid residue led to different loading efficiencies, highlighting the tunability of the system. We note that only the anionic peptides have the capability to load transition metal complexes at appreciable levels, likely due to electrostatic repulsions with the oxidized metal-center. Drug-loaded anionic peptide nanofilaments showed a substantial cytotoxicity increase toward cancerous cells *in vitro* compared to the free drugs (up to 15-fold in Caki-1, and up to 5-fold in MDA-MB-231). Relevantly, the selectivity toward the cancerous cells compared to non-tumorigenic IMR-90, increased considerably (up to 16-fold for compound **1** and up to 12-fold for **2**). This increase in selectivity suggests that MMPs and potentially other proteases responsible for the enhanced proteolytic activity surrounding cancer cells facilitate filament breakdown and uptake of drug-bound peptide fragments. Peptides are nontoxic to cells at low concentrations (though we note that just 1 mM is sufficient to encapsulate enough payload to achieve significant cell death), and they are inherently biocompatible and biodegradable. This can be seen as a proof-of-concept of self-assembled peptide filaments as locally degradable delivery vehicles for transition metal-based complexes. While originally designed to be MMP-9 responsive, we propose that a more general targeting of regions with high protease activity provides a more general route to targeted delivery of anticancer agents, and that drug binding to hydrophobic peptide fragments may generally assist availability of poorly soluble drugs.

EXPERIMENTAL SECTION

Coarse Grained Molecular Dynamics Simulations. The 4 peptide sequences were converted to extended atomistic structure PDB files using PyMOL which were subsequently used to generate the MARTINI 2.1 Force-Field[89,90] compliant topology files using the martinize.py script. The extended beta-sheet secondary structure was selected during this atomistic to coarse-grained conversion, and the termini and side chains were ionized in their standard states. 950 of these coarse-grained peptide structures were subsequently inserted in random configurations into a $25 \times 25 \times 25$ nm^3 box using *gmx insert-molecules* leading to an effective concentration of ∼100 mM. This peptide box was then solvated using MARTINI water and the *gmx solvate* tool. 1900 MARTINI ions (Na^+ or Cl^-) were added to neutralize the box (since each peptide has a +2/−2 charge) using the *gmx genion* tool. These solvated and neutralized boxes were subjected to a steepest descent energy minimization and a 1 ns *NPT* equilibration at 298 K and 1.0 bar reference temperature and pressure respectively using a 10 fs time step to remove packing conflicts and solvent configuration instabilities. 5000 ns (5 μs) production runs were carried out using the GROMACS 2021.5 package[91] using a 20 fs time step with a Verlet algorithm. A 1.1 nm coulomb cutoff was used along with the Reaction-Field treatment of Coulombic interactions. Van der Waals interactions were incorporated using a 1.1 nm vdW cutoff. Temperature coupling to 298 K was achieved through velocity rescaling,[92] and Parrinello−Rahman pressure coupling was used to maintain 1 bar with a tau-p of 12. LINCS was used as the constraint algorithm of choice.[93] Solvent Accessible Surface Areas were computed using *gmx sasa* by specifying a solvent probe radius of 0.4 nm.[94] Peptide structures and trajectories were visualized and rendered using VMD.[95]

Gold Complexes. Gold compounds **1** and **2** were prepared as previously reported.[69,70] Chemicals were purchased as indicated: $H[AuCl_4]$ (Strem Chemicals, Newburyport, MA), benzyl bromide, ethyl iodide, and silver oxide (Sigma-Aldrich, St. Louis, MO), 4,5-diphenylimizadole and lithium bis(trimethylsilyl)amide (Alfa Aesar, Haverhill, MA). Reaction solvents were purchased anhydrous from Fisher Scientific (BDH, ACS grade) and Sigma-Aldrich, used without further purification, dried in a SPS machine, and kept over molecular sieves (3 Å, beads, 4−8 mesh), otherwise over sodium if necessary. Deuterated solvents were purchased from Cambridge Isotope Laboratories, Inc., and were kept over molecular sieves (3 Å, beads, 4−8 mesh). Celite (Celite 545, Diatomaceous Earth) was purchased from VWR International and used as received.

Solid Phase Peptide Synthesis. Fluorenylmethyloxycarbonyl (Fmoc)-protected amino acids and preloaded Wang resins were purchased from Bachem. Peptides were synthesized on CEM Liberty Blue microwave-assisted solid phase peptide synthesizer using ∼1:5 resin to amino acid ratio and excess diisopropylcarbodiimide, Oxyma (ethyl(hydroxyamino)cyanoacetate), and 20% piperidine in dimethylformamide (DMF). The complete peptide loaded resins were washed three times in dichloromethane, followed by three washes in diethyl ether on a filtration column. The peptides were cleaved from resins, and side chain protecting groups were removed by reacting

https://doi.org/10.1021/jacs.2c09820
J. Am. Chem. Soc. 2023, 145, 234−246

with a TFA cocktail (95% trifluoroacetic acid (TFA), 2.5% triisopropylsilane (TIS), and 2.5% water) for 2 h. The cleaved peptides were recovered by removing TFA cocktail, followed by precipitation in cold diethyl ether, using a centrifuge to decant the supernatant. The crude peptides were dissolved in Milli-Q water and lyophilized.

Preparatory High-Performance Liquid Chromatography. Lyophilized crude peptides were dissolved in 50% acetonitrile in water containing 0.1% formic acid (FA) and purified through a preparatory C_{18} column on a Thermo Scientific Dionex Ultimate 3000. Acetonitrile was removed from the collected fragments on a rotary evaporator before lyophilization.

Removal of TFA Counterions. Purified peptides were dissolved in 10 mM HCl solution to make 1 mM peptide solution and lyophilized to remove residual TFA. Washed peptides were characterized using ^{19}F NMR.

Peptide Stability in Buffer. Peptide solutions (1 mM) were prepared in 10 mM phosphate buffer, and pH adjusted to 7.4 using dilute HCl or NaOH. Peptides were incubated at 37 °C in a stationary heat block, samples were taken every 24 h for LC-MS analysis. Thirty μL of the peptide solution was directly added to 270 μL 50% acetonitrile in water containing 0.1% FA. Samples were analyzed on a LC-MS system comprised of an Agilent 1200 LC system coupled to an Agilent 6340 ion trap mass spectrometer. Samples (4 μL) were injected onto a Phenomenex Luna Omega column (C18, 50 × 2.1 mm) using a gradient of 2.5−95% acetonitrile in water (0.1% formic acid) at a flow rate of 0.300 mL/min over 7.5 min followed by a 1 min wash step with 95% acetonitrile. MS was warmed up prior to sample for injection for 1.5 h. (RT = 6.57 min (**PD**), 6.31 min (**AD**), 5.86 min (**PK**), 5.80 min (**AK**)). Remaining peptides were quantified by comparing the peak area to the area at t = 0.

Critical Aggregation Concentration. Drug-loaded peptide solutions (1 mM) were prepared in 10 mM phosphate buffer, and the pH was adjusted to 7.4 using 0.5 M NaOH or 0.5 M HCl and serially diluted in 10 mM phosphate buffer with thorough vortexing. Peptide solutions were incubated in 50 °C for 15 min, then 2 μL of stock pyrene solution (100 μM in methanol) was added to 100 μL of each peptide solution, gently mixed, and incubated for 5 min at 50 °C, and then finally cooled to room temperature to coassemble the peptides with pyrene molecules. Pyrene emission spectra were measured from 350 to 450 nm (λ_{ex} = 310 nm) in a microfluorescence cuvette (3 mm path length) on a Jasco FP-8500 spectrofluorometer (measurement parameters: 20 nm excitation and 1 nm emission bandwidth, 0.2 s response, medium sensitivity, 0.2 nm data interval, at 200 nm/min). The CAC was determined by plotting the ratio between intensities of the third to first peak of the pyrene emission spectra. Increasing peptide concentrations were measured in 0.1 mM increments until the slope of the plot had changed.

Fourier Transform-Infrared Spectroscopy. Absorbance spectra were taken on a Bruker Vertex 70 spectrometer from 4000 to 800 cm^{-1} with 64 scans at 4 cm^{-1} resolution. Peptide solutions (20 mM) in deuterated phosphate buffer were prepared and pH adjusted to 7.4, then sonicated for 10 min. Five μL of peptide solution was drop casted between two CaF2 cells with PTFE spacers (12 μM thickness × 13 mm diameter).

Encapsulation Method. Two mM peptide stock solutions were prepared in deionized water. Stock gold-based compound solutions were prepared in acetonitrile. In 1.5 mL centrifugal tubes, 100 μL of peptide solution was combined with 100 μL of gold-compound solution for a final concentration of 1 mM peptide in a 1:1 ratio of water and acetonitrile. Solution was vortexed thoroughly and sonicated for 20 min, followed by concentration under reduced pressure. The resulting dried film was reconstituted in 200 μL of 10 mM phosphate buffer and pH adjusted to 7.4 using 0.5 M NaOH and 0.5 M HCl in order to suspend the peptide-gold compound mixture. Then, the mixture was gently vortexed and sonicated for 20 min. Nonencapsulated hydrophobic gold compound was separated from suspended peptide-gold compound nanocarriers via centrifugation (10^4 rpm, 1 min). 200 μL of supernatant were collected for analysis and characterization.

Gold Quantification. Analysis was carried out using a PerkinElmer Analyst 800 using a transversely heated graphite atomizer (THGA) furnace system at 242.8 nm. Sample aliquots were digested in concentrated nitric acid (70%), refluxed for 2 h, and then to dryness, and redissolution in adequate volumes of 10% hydrochloric acid solution to be within the calibration curve range. Calibration solutions were prepared from gold standard solution in 10% hydrochloric acid. Calibration curve was linear over the 10−100 ppb range (r^2 = 0.997).

Zeta Potential. Zeta-potential measurements were made on an Anton Paar Litesizer 500 Particle Analyzer. Peptide samples (1 mM) were prepared in 10 mM phosphate buffer, and the pH was adjusted to 7.4 using dilute NaOH and HCl. 65 μL of sample was pipetted into a Univette low volume cuvette, and three series of measurements were made at 25 °C using Smoluchowski approximation.

Atomic Force Microscopy. AFM images were taken on Bruker Dimension FastScan using FASTSCAN-B tip on fast scan mode. Peptide solution (1 mM) was prepared in phosphate buffer (pH 7.4) sonicated for 10 min and drop casted on freshly cleaved mica and allowed to dry for 72 h before imaging.

Transmission Electron Microscopy. TEM images were taken on FEI Tecnai G2 Spirit Twin TEM. Peptides and drug-loaded peptide solutions (1 mM) were prepared in 10 mM phosphate buffer (pH 7.4) and 5 μL was drop casted on a carbon film grid (400 mesh, copper) and dried completely. To the dry grid was added 5 μL of Milli-Q water and quickly blotted to wash away the phosphate salts and dried completely. Finally, 5 μL of methylamine vanadate based negative stain (NanoVan by Nanoprobes) was drop casted, blotted away, and dried completely.

Cell Culture. Human breast adenocarcinoma line MDA-MB-231 and human lung fibroblast line IMR-90 were obtained from the American Type Culture Collection (ATCC; Manassas, Virginia, USA) and cultured with Dulbecco's modified Eagle's medium (DMEM; Fisher Scientific) containing 10% fetal bovine serum, certified, heat inactivated, US origin (FBS; Fisher Scientific), 1% minimum essential media (MEM) nonessential amino acids (NEAA; Fisher Scientific), and 1% penicillin−streptomycin (PenStrep; Fisher Scientific). Human clear cell renal cell carcinoma Caki-1 line was cultured using Roswell Park Memorial Institute (RPMI-1640; Fisher Scientific, Hampton, NH, USA) and supplemented with 10% FBS, 1% MEM-NEAA, and 1% PenStrep. All cells were cultured at 37 °C under 5% CO_2 and 95% air in a humidified incubator.

MMP-9 Expression in Media and Cells. Cells and media were collected in falcon tubes and centrifuged. Supernatant was transferred to a new falcon tube and cells were washed with PBS and centrifuged. Equivalent amounts of total protein from cells or media (100 μg) per cell line were used to measure MMP-9 levels. MMP-9 expression was performed using a commercial kit (Human MMP-9 ELISA Kit, BMS2016-2, ThermoFisher, Waltham, MA) according to the manufacturer's instructions. MMP-9 expression is presented as a mean ± SD of two independent experiments.

Expression in Cells. Cells were lysed (4 °C, 1 h) with RIPA buffer (50 mM Tris-Cl, 150 mM NaCl, 1% NP-40 (Igepal CA-630, Sigma-Aldrich, St. Louis, MO), 0.5% Sodium Deoxycholate, 0.1% SDS, 1 mM DTT) containing a protease and phosphatase inhibitor cocktail (Roche, Basel, Switzerland). Lysates were centrifuged (14 000g, 5 min), and total protein concentration was measured by Bradford assay.

Expression in Media. Media was filtrated through 50K cutoff filters (Amicon Ultra-15 Centrifugal Filter Units, MilliporeSigma, Burlington, MA) according to the manufacturer's instructions. Only proteins with molecular weights higher than 50 kDa were used for MMP-9 expression assays.

Gelatin Zymography. Cells were cultured in standard conditions with serum-containing medium. At 70−80% confluency, FBS media was removed. Cells were washed twice with FBS-free media and incubated with serum-free medium for 24 h. After incubation, conditioned media was collected, and cells were washed with PBS. Cell pellets were lysed (4 °C, 1 h) with RIPA buffer (50 mM Tris-Cl, 150 mM NaCl, 1% NP-40 (Igepal CA-630, Sigma-Aldrich, St. Louis,

https://doi.org/10.1021/jacs.2c09820
J. Am. Chem. Soc. 2023, 145, 234−246

MO), 0.5% Sodium Deoxycholate, 0.1% SDS, 1 mM DTT). Media was filtered through 50K cutoff filters (Amicon Ultra-15 Centrifugal Filter Units, MilliporeSigma, Burlington, MA) according to the manufacturer's instructions. Equivalent amounts of total protein from cells and media (100 μg) were loaded in a 7.5% acrylamide that has been copolymerized with 4 mg/mL gelatin. Upon electrophoresis, gels were washed twice for 30 min at room temperature with washing buffer (2.5% Triton X-100, 50 mM Tris HCl, 5 mM $CaCl_2$, and 1 μM $ZnCl_2$ at pH 7.5) and then incubated overnight at 37 °C with the incubation buffer (1% Triton X-100, 50 mM Tris HCl, 5 mM $CaCl_2$, and 1 μM $ZnCl_2$ at pH 7.5). The bands of gelatinolytic activity were revealed after staining the gels with Coomassie blue (0.5% w/v Comassie Brilliant Blue, Biorad). Band intensity was analyzed with ImageJ (version 1.52a).

MMP-9 Inhibition. After 24 h of seeding, cells were treated with corresponding compounds (**1** and **2**) or vehicle control at IC_{20} concentrations and collected after 72 h. Cells were then lysed (4 °C, 1 h) with RIPA buffer (50 mM Tris-Cl, 150 mM NaCl, 1% NP-40 (Igepal CA-630, Sigma-Aldrich, St. Louis, MO), 0.5% Sodium Deoxycholate, 0.1% SDS, 1 mM DTT) containing a protease and phosphatase inhibitor cocktail (Roche, Basel, Switzerland). Lysates were centrifuged (14 000*g*, 5 min), and total protein concentration was measured by Bradford assay. Equivalent amounts of total protein from cells or media (100 μg) per cell line were used in order to measure MMP-9 levels. MMP-9 expression was performed using a commercial kit (Human MMP-9 ELISA Kit, BMS2016-2, ThermoFisher, Waltham, MA) according to the manufacturer's instructions. MMP-9 expression is presented as a mean ± SD. Experiments were carried out in triplicate.

Cell Viability Analysis. The cytotoxic profile of the compounds was determined by assessing the viability of MDA-MB-231, Caki-1, and IMR-90 cell lines. Cells were seeded at a concentration of 5.6×10^3 to 6×10^3 cells per well in 90 μL of appropriate complete media into tissue-culture-grade 96-well flat-bottom microplates (CELLTREAT, Pepperell, MA, USA) and grown for 24 h at 37 °C under 5% CO_2 and 95% air in a humidified incubator. Compound **1** was dissolved in a 1:1 solution of Triethylglycol and DMSO, while compound **2** was dissolved in DMSO. **PD+1**, **PD+2**, **AD+1**, **AD+2** were provided in buffer solution with the concentration of encapsulated payload, previously calculated via AAS. PrestoBlue was used to quantitatively measure variations in the viability of treated cells. Eleven μL per well of 10× PrestoBlue (Invitrogen, Carlsbad, CA, USA) labeling mixture was added to the cells at a final concentration of 1× and incubated for 1 h at 37 °C under 5% CO_2 and 95% air in a humidified incubator following 72-h exposure to peptides. The optical fluorescence of each well in a 96-well plate was quantified using a BioTek Synergy Multimode microplate reader (BioTek Instruments, Inc., Winooski, VT, USA) set at 560/590 nm. The percentage of surviving cells was calculated from the ratio of absorbance of treated to untreated cells in least two independent experiments, each with triplicate measurements. All data presented are expressed as the mean ± standard deviation.

MMP-9 Kinetics and Payload Release. *MMP-9 Kinetics.* Drug-loaded peptide solutions (1 mM) in PBS supplemented with $CaCl_2$, $ZnCl_2$ were incubated with 100 ng/mL MMP-9 (human, catalytic domain) at 37 °C in a stationary heat block for 72 h. At each time point, 30 μL of peptide solution was directly added to 270 μL 50% acetonitrile solution containing 0.1% FA. Samples were analyzed on an LC-MS system comprised of an Agilent 1200 LC system coupled to an Agilent 6340 ion trap mass spectrometer. Samples (3 μL) were injected onto a Phenomenex Luna Omega column (C18, 50 × 2.1 mm) using a gradient of 2.5−95% acetonitrile in water (0.1% FA) at a flow rate of 0.300 mL/min over 7.5 min followed by a 1 min wash step with 95% acetonitrile.

Payload Release. At each time point, reaction samples were centrifuged at 10^4 rpm for 1 min, and supernatant was collected. Drug-loaded peptides in supernatant were digested using concentrated nitric acid and quantified using AAS at 242.8 nm and compared to quantification at $t = 0$.

Incubation with Media. Media was incubated with cancerous and noncancerous cell lines for 24 h before subsequent centrifugation and removal of cells. Peptide solutions (1 mM) were incubated in the resulting media (using standard media as a control) at 37 °C in a stationary heat block for 72 h. Every 24 h, 30 μL of peptide solution was directly added to 270 μL 50% acetonitrile solution containing 0.1% FA. Samples were analyzed on an LC-MS system comprised of an Agilent 1200 LC system coupled to an Agilent 6340 ion trap mass spectrometer. Samples (3 μL) were injected onto a Phenomenex Luna Omega column (C18, 50 × 2.1 mm) using a gradient of 2.5−95% acetonitrile in water (0.1% FA) at a flow rate of 0.300 mL/min over 7.5 min followed by a 1 min wash step with 95% acetonitrile. Remaining peptides were quantified by comparing the peak area to the area at $t = 0$.

Cell Organelle Uptake Studies. To determine the gold metal uptake in Caki-1, cells were seeded onto a 6 well plate (Corning) at a density of 25×10^3. Following 24 h incubation with peptides, incubation, subcellular fractionation buffer (20 mM HEPES pH 7.4, 10 mM KCl, 2 mM $MgCl_2$, 1 mM EDTA, 1 mM EGTA, 1 mM DTT, protease inhibitor cocktail) was added and the cell suspension was passed through a 27-gauge needle 10 times to lyse cells. Cells were incubated on ice for 20 min and then centrifuged at 720*g* for 5 min. The supernatant was collected, which contained cytoplasm and mitochondrial components. The cell pellet, containing the nuclear fragment, was further passed through a 25-gauge needle with 500 μL fractionation buffer 10 times and then centrifuged for 10 min at 720*g*. The supernatant containing mitochondrial and cytoplasm components was centrifuged for 5 min at 10 000*g*. The subsequent supernatant was collected as the cytoplasmic fraction, and the cell pellet was collected for the mitochondrial fragment. The nuclear and mitochondrial fractions were resuspended in TBS with 0.1% SDS and then sonicated to homogenize the lysates. Sample aliquots were digested in concentrated nitric acid (70%), refluxed for 2 h, and then to dryness, and redissolution in adequate volumes of 10% hydrochloric acid solution to be within the calibration curve range. Analysis was carried out using a PerkinElmer Analyst 800 using a transversely heated graphite furnace (THGA) system at 242.8 nm. Biodistribution values are presented as the percent of the accumulated dose and were calculated by including appropriate standards. All data presented are expressed as mean ± SD. All samples were completed in triplicate.

Cell Death Type Assay. Cells were cultured in 100 mm tissue culture dishes with RPMI media. Following cell confluency reaching ≈75%, cells were treated with 0.1% DMSO vehicle control, **1** (1 μM), and **PD+1** (1 mM **PD** + 1 μM **1**) and incubated for 72 h at 37 °C under 5% CO_2 and 95% air in a humidified incubator. Then, cells were collected through trypsinization to later count with a hemocytometer and prepare 2.5×10^4 cells per sample. After the samples were prepared, two cold PBS washes were completed. Once PBS was aspirated out, the BD Pharmigen FITC Annexin V Apoptosis Detection Kit 1eBioscience Annexin V-FITC Apop Kit (BD Biosciences, San Diego, California) was used to label cells as follows: Cells were resuspended in 100 μL 1× binding buffer with 5 μL Annexin V dye and 5 μL propidium iodide. The cells were incubated at room temperature in the dark for 15 min. After the incubation period, cells were resuspended in 400 μL 1× binding buffer. The dye's fluorescence intensity was detected via flow cytometry using a BD C6 Accuri flow cytometer; 10×10^5 events per sample were recorded. The flow cytometer was calibrated prior to each use.

■ ASSOCIATED CONTENT

Supporting Information

The Supporting Information is available free of charge at https://pubs.acs.org/doi/10.1021/jacs.2c09820.

MD simulations, peptide stability, drug loading, characterization using ζ-potential, AFM, TEM, MMP-9 expression and activity, cell viability, enzyme kinetics and drug release, cellular uptake, cell death (PDF)

https://doi.org/10.1021/jacs.2c09820
J. Am. Chem. Soc. 2023, 145, 234−246

Movie S1: 5000 ns coarse-grained molecular dynamics trajectory of 950 copies of the **PD** peptide with water and ion beads removed for clarity; Snapshots were saved every nanosecond, and the peptide beads are color coded with purple for FF beads, green for PLGLAG beads, and red for the DD beads (MPG)

Movie S2: 5000 ns coarse-grained molecular dynamics trajectory of 950 copies of the **PK** peptide with water and ion beads removed for clarity; Snapshots were saved every nanosecond, and the peptide beads are color coded with purple for FF beads, green for PLGLAG beads, and blue for the KK beads (MPG)

Movie S3: 5000 ns coarse-grained molecular dynamics trajectory of 950 copies of the **AD** peptide with water and ion beads removed for clarity; Snapshots were saved every nanosecond, and the peptide beads are color coded with purple for FF beads, green for ALGLAG beads, and red for the DD beads (MPG)

Movie S4: 5000 ns coarse-grained molecular dynamics trajectory of 950 copies of the **AK** peptide with water and ion beads removed for clarity; Snapshots were saved every nanosecond, and the peptide beads are color coded with purple for FF beads, green for ALGLAG beads, and blue for the KK beads (MPG)

AUTHOR INFORMATION

Corresponding Authors

María Contel − *Department of Chemistry, Brooklyn College, CUNY, Brooklyn, New York 11210, United States; Ph.D. Program in Chemistry, Ph.D. Program in Biochemistry, and Ph.D. Program in Biology, The Graduate Center of CUNY, New York, New York 10016, United States;* orcid.org/0000-0002-9825-4441; Email: mariacontel@brooklyn.cuny.edu

Rein V. Ulijn − *Nanoscience Initiative, Advanced Science Research Center at The Graduate Center of the City University of New York (CUNY), New York, New York 10031, United States; Ph.D. Program in Chemistry and Ph.D. Program in Biochemistry, The Graduate Center of CUNY, New York, New York 10016, United States; Department of Chemistry, Hunter College, CUNY, New York, New York 10065, United States;* orcid.org/0000-0002-7138-1213; Email: rulijn@gc.cuny.edu

Authors

Yaron Marciano − *Nanoscience Initiative, Advanced Science Research Center at The Graduate Center of the City University of New York (CUNY), New York, New York 10031, United States; Department of Chemistry, Brooklyn College, CUNY, Brooklyn, New York 11210, United States; Ph.D. Program in Chemistry, The Graduate Center of CUNY, New York, New York 10016, United States*

Virginia del Solar − *Department of Chemistry, Brooklyn College, CUNY, Brooklyn, New York 11210, United States;* Present Address: Cell and Gene Therapy Catapult, 12th Floor Tower Wing, Guy's Hospital, Great Maze Pond, London SE1 9RT, United Kingdom

Nazia Nayeem − *Department of Chemistry, Brooklyn College, CUNY, Brooklyn, New York 11210, United States; Ph.D. Program in Biology, The Graduate Center of CUNY, New York, New York 10016, United States*

Dhwanit Dave − *Nanoscience Initiative, Advanced Science Research Center at The Graduate Center of the City University of New York (CUNY), New York, New York 10031, United States; Ph.D. Program in Chemistry, The Graduate Center of CUNY, New York, New York 10016, United States; Department of Chemistry, Hunter College, CUNY, New York, New York 10065, United States;* orcid.org/0000-0002-6218-4584

Jiye Son − *Nanoscience Initiative, Advanced Science Research Center at The Graduate Center of the City University of New York (CUNY), New York, New York 10031, United States;* orcid.org/0000-0003-3482-9813

Complete contact information is available at: https://pubs.acs.org/10.1021/jacs.2c09820

Notes

The authors declare no competing financial interest.

ACKNOWLEDGMENTS

This work was supported by the National Institute of General Medical Sciences through Grant 2SC1GM127278-07A1 (to M.C.). We thank the CUNY-Advanced Science Research center for a SEED grant (to M.C.) and the Graduate Research Technology Initiative Fund Round 21 Supplement from CUNY for funds to purchase a plate reader (to M.C.). R.V.U. and D.D. acknowledge funding from the Office of Naval Research for the Vannevar Bush Faculty Fellowship (Grant N00014-21-1-2967) and Air Force Office of Scientific Research (Grant No. FA9550-21-1-0091). D.D. would like to acknowledge computing resources and time from the City University of New York High Performance Computing Center under NSF grants CNS-0855217, CNS-0958379, ACI-1126113, and OEC-2215760 (2022). We acknowledge Mike Cornejo for preliminary biological results, Lina Alhanshali for assisting with AAS measurements, and Scott McPhee for assistance with the peptide synthesizer, HPLC, and LC-MS.

REFERENCES

(1) Wang, J.; Li, Y.; Nie, G. Multifunctional Biomolecule Nanostructures for Cancer Therapy. *Nat. Rev. Mater.* **2021**, *6* (9), 766−783.

(2) Mitragotri, S.; Anderson, D. G.; Chen, X.; Chow, E. K.; Ho, D.; Kabanov, A. V.; Karp, J. M.; Kataoka, K.; Mirkin, C. A.; Petrosko, S. H.; Shi, J.; Stevens, M. M.; Sun, S.; Teoh, S.; Venkatraman, S. S.; Xia, Y.; Wang, S.; Gu, Z.; Xu, C. Accelerating the Translation of Nanomaterials in Biomedicine. *ACS Nano* **2015**, *9* (7), 6644−6654.

(3) Yang, W.; Veroniaina, H.; Qi, X.; Chen, P.; Li, F.; Ke, P. C. Soft and Condensed Nanoparticles and Nanoformulations for Cancer Drug Delivery and Repurpose. *Adv. Ther (Weinh)* **2020**, *3* (1), 1900102.

(4) Kinnear, C.; Moore, T. L.; Rodriguez-Lorenzo, L.; Rothen-Rutishauser, B.; Petri-Fink, A. Form Follows Function: Nanoparticle Shape and Its Implications for Nanomedicine. *Chem. Rev.* **2017**, *117* (17), 11476−11521.

(5) Hou, X.; Zaks, T.; Langer, R.; Dong, Y. Lipid Nanoparticles fr MRNA Delivery. *Nat. Rev. Mater.* **2021**, *6* (12), 1078−1094.

(6) Zhang, S. Fabrication of Novel Biomaterials through Molecular Self-Assembly. *Nat. Biotechnol.* **2003**, *21* (10), 1171−1178.

(7) Cui, H.; Webber, M. J.; Stupp, S. I. Self-Assembly of Peptide Amphiphiles: From Molecules to Nanostructures to Biomaterials. *Pept Sci.* **2010**, *94* (1), 1−18.

(8) Lopez-Silva, T. L.; Schneider, J. P. From Structure to Applicatin: Progress and Opportunities in Peptide Materials Development. *Curr. Opin Chem. Biol.* **2021**, *64*, 131−144.

(9) Blum, A. P.; Kammeyer, J. K.; Rush, A. M.; Callmann, C. E.; Hahn, M. E.; Gianneschi, N. C. Stimuli-Responsive Nanomaterials for

Biomedical Applications. *J. Am. Chem. Soc.* **2015**, *137* (6), 2140−2154.
(10) Soukasene, S.; Toft, D. J.; Moyer, T. J.; Lu, H.; Lee, H.-K. K.; Standley, S. M.; Cryns, V. L.; Stupp, S. I. Antitumor Activity of Peptide Amphiphile Nanofiber-Encapsulated Camptothecin. *ACS Nano* **2011**, *5* (11), 9113−9121.
(11) Mura, S.; Nicolas, J.; Couvreur, P. Stimuli-Responsive Nanocarriers for Drug Delivery. *Nat. Mater.* **2013**, *12* (11), 991−1003.
(12) Koren, E.; Apte, A.; Jani, A.; Torchilin, V. P. Multifunctional PEGylated 2C5-Immunoliposomes Containing PH-Sensitive Bonds and TAT Peptide for Enhanced Tumor Cell Internalization and Cytotoxicity. *J. Controlled Release* **2012**, *160* (2), 264−273.
(13) Shahriari, M.; Zahiri, M.; Abnous, K.; Taghdisi, S. M.; Ramezani, M.; Alibolandi, M. Enzyme Responsive Drug Delivery Systems in Cancer Treatment. *J. Controlled Release* **2019**, *308*, 172−189.
(14) Lee, J. S.; Groothuis, T.; Cusan, C.; Mink, D.; Feijen, J. Lysosomally Cleavable Peptide-Containing Polymersomes Modified with Anti-EGFR Antibody for Systemic Cancer Chemotherapy. *Biomaterials* **2011**, *32* (34), 9144−9153.
(15) Son, J.; Kalafatovic, D.; Kumar, M.; Yoo, B.; Cornejo, M. A.; Contel, M.; Ulijn, R. V. Customizing Morphology, Size, and Response Kinetics of Matrix Metalloproteinase-Responsive Nanostructures by Systematic Peptide Design. *ACS Nano* **2019**, *13*, 1555−1562.
(16) Kalafatovic, D.; Nobis, M.; Javid, N.; Frederix, P. W. J. M.; Anderson, K. I.; Saunders, B. R.; Ulijn, R. V. MMP-9 Triggered Micelle-to-Fibre Transitions for Slow Release of Doxorubicin. *Biomater Sci.* **2015**, *3* (2), 246.
(17) Mason, S. D.; Joyce, J. A. Proteolytic Networks in Cancer. *Trends Cell Biol.* **2011**, *21* (4), 228−237.
(18) Zelzer, M.; Todd, S. J.; Hirst, A. R.; McDonald, T. O.; Ulijn, R. V. Enzyme Responsive Materials: Design Strategies and Future Developments. *Biomater. Sci.* **2013**, *1* (1), 11−39.
(19) Li, J.; Xu, B. Enzyme-Mediated Self-Assembly. *Self-Assembling Biomaterials: Molecular Design, Characterization and Application in Biology and Medicine* **2018**, 399−417.
(20) Zhou, J.; Xu, B. Enzyme-Instructed Self-Assembly: A Multistep Process for Potential Cancer Therapy. *Bioconjug Chem.* **2015**, *26* (6), 987−999.
(21) Lutolf, M. P.; Hubbell, J. A. Synthetic Biomaterials as Instructive Extracellular Microenvironments for Morphogenesis in Tissue Engineering. *Nat. Biotechnol.* **2005**, *23* (1), 47−55.
(22) West, J. L.; Hubbell, J. A. Polymeric Biomaterials with Degradation Sites for Proteases Involved in Cell Migration. *Macromolecules* **1999**, *32* (1), 241−244.
(23) Patterson, J.; Hubbell, J. A. Enhanced Proteolytic Degradation of Molecularly Engineered PEG Hydrogels in Response to MMP-1 and MMP-2. *Biomaterials* **2010**, *31* (30), 7836−7845.
(24) Tanaka, A.; Fukuoka, Y.; Morimoto, Y.; Honjo, T.; Koda, D.; Goto, M.; Maruyama, T. Cancer Cell Death Induced by the Intracellular Self-Assembly of an Enzyme-Responsive Supramolecular Gelator. *J. Am. Chem. Soc.* **2015**, *137* (2), 770−775.
(25) Zhou, J.; Du, X.; Yamagata, N.; Xu, B. Enzyme-Instructed Self-Assembly of Small D-Peptides as a Multiple-Step Process for Selectively Killing Cancer Cells. *J. Am. Chem. Soc.* **2016**, *138* (11), 3813−3823.
(26) Callmann, C. E.; Barback, C. V.; Thompson, M. P.; Hall, D. J.; Mattrey, R. F.; Gianneschi, N. C. Therapeutic Enzyme-Responsive Nanoparticles for Targeted Delivery and Accumulation in Tumors. *Adv. Mater.* **2015**, *27* (31), 4611−4615.
(27) Lin, Y.-A.; Ou, Y.-C.; Cheetham, A. G.; Cui, H. Rational Design of MMP Degradable Peptide-Based Supramolecular Filaments. *Biomacromolecules* **2014**, *15* (4), 1419−1427.
(28) Kulkarni, P. S.; Haldar, M. K.; Nahire, R. R.; Katti, P.; Ambre, A. H.; Muhonen, W. W.; Shabb, J. B.; Padi, S. K. R.; Singh, R. K.; Borowicz, P. P.; Shrivastava, D. K.; Katti, K. S.; Reindl, K.; Guo, B.; Mallik, S. MMP-9 Responsive PEG Cleavable Nanovesicles for Efficient Delivery of Chemotherapeutics to Pancreatic Cancer. *Mol. Pharmaceutics* **2014**, *11* (7), 2390−2399.
(29) Kim, K.; Bae, B.; Kang, Y. J.; Nam, J.-M.; Kang, S.; Ryu, J.-H. Natural Polypeptide-Based Supramolecular Nanogels for Stable Noncovalent Encapsulation. *Biomacromolecules* **2013**, *14* (10), 3515−3522.
(30) Kalafatovic, D.; Nobis, M.; Son, J.; Anderson, K. I.; Ulijn, R. V. MMP-9 Triggered Self-Assembly of Doxorubicin Nanofiber Depots Halts Tumor Growth. *Biomaterials* **2016**, *98*, 192−202.
(31) Lu, Y.; Aimetti, A. A.; Langer, R.; Gu, Z. Bioresponsive Materials. *Nat. Rev. Mater.* **2017**, *2* (1), 1−17.
(32) Li, M.; Zhao, G.; Su, W. K.; Shuai, Q. Enzyme-Responsive Nanoparticles for Anti-Tumor Drug Delivery. *Front Chem.* **2020**, *8*, 647.
(33) Battistella, C.; Liang, Y.; Gianneschi, N. C. Innovations in Disease State Responsive Soft Materials for Targeting Extracellular Stimuli Associated with Cancer, Cardiovascular Disease, Diabetes, and Beyond. *Adv. Mater.* **2021**, *33* (46), 2007504.
(34) Qu, M.; Jiang, X.; Zhou, X.; Wang, C.; Wu, Q.; Ren, L.; Zhu, J.; Zhu, S.; Tebon, P.; Sun, W.; Khademhosseini, A. Stimuli-Responsive Delivery of Growth Factors for Tissue Engineering. *Adv. Healthc Mater.* **2020**, *9* (7), 1901714.
(35) Lutolf, M. P.; Lauer-Fields, J. L.; Schmoekel, H. G.; Metters, A. T.; Weber, F. E.; Fields, G. B.; Hubbell, J. A. Synthetic Matrix Metalloproteinase-Sensitive Hydrogels for the Conduction of Tissue Regeneration: Engineering Cell-Invasion Characteristics. *Proc. Natl. Acad. Sci. U. S. A.* **2003**, *100* (9), 5413−5418.
(36) Cancemi, P.; Buttacavoli, M.; Roz, E.; Feo, S. Expression of Alpha-Enolase (ENO1), Myc Promoter-Binding Protein-1 (MBP-1) and Matrix Metalloproteinases (MMP-2 and MMP-9) Reflect the Nature and Aggressiveness of Breast Tumors. *Int. J. Mol. Sci.* **2019**, *20* (16), 3952.
(37) Sumi, T.; Nakatani, T.; Yoshida, H.; Hyun, Y.; Yasui, T.; Matsumoto, Y.; Nakagawa, E.; Sugimura, K.; Kawashima, H.; Ishiko, O. Expression of Matrix Metalloproteinases 7 and 2 in Human Renal Cell Carcinoma. *Oncol. Rep.* **2003**, *10* (3), 567−570.
(38) Lehmann, B. D.; Jovanović, B.; Chen, X.; Estrada, M. V.; Johnson, K. N.; Shyr, Y.; Moses, H. L.; Sanders, M. E.; Pietenpol, J. A. Refinement of Triple-Negative Breast Cancer Molecular Subtypes: Implications for Neoadjuvant Chemotherapy Selection. *PLoS One* **2016**, *11* (6), No. e0157368.
(39) del Solar, V.; Contel, M. Metal-Based Antibody Drug Conjugates. Potential and Challenges in Their Application as Targeted Therapies in Cancer. *J. Inorg. Biochem* **2019**, *199*, 110780.
(40) Nayeem, N.; Contel, M. Exploring the Potential of Metallodrugs as Chemotherapeutics for Triple Negative Breast Cancer. *Chem. Eur. J.* **2021**, *27* (35), 8891−8917.
(41) Caulfield, S. E.; Davis, C. C.; Byers, K. F. Olaparib: A Novel Therapy for Metastatic Breast Cancer in Patients With a BRCA1/2 Mutation. *J. Adv. Pract. Oncol.* **2019**, *10* (2), 167−174.
(42) Margulis, V.; Tamboli, P.; Matin, S. F.; Meisner, M.; Swanson, D. A.; Wood, C. G. Redefining PT3 Renal Cell Carcinoma in the Modern Era. *Cancer* **2007**, *109* (12), 2439−2444.
(43) Siegel, R. L.; Miller, K. D.; Jemal, A. Cancer Statistics, 2017. *CA Cancer J. Clin.* **2017**, *67* (1), 7−30.
(44) Serzan, M. T.; Atkins, M. B. Current and Emerging Therapies for First Line Treatment of Metastatic Clear Cell Renal Cell Carcinoma. *J. Cancer Metastasis Treat.* **2021**, *7*, 39.
(45) Stadler, W. M.; Halabi, S.; Rini, B.; Ernstoff, M. S.; Davila, E.; Picus, J.; Barrier, R.; Small, E. J. A Phase II Study of Gemcitabine and Capecitabine in Metastatic Renal Cancer. *Cancer* **2006**, *107* (6), 1273−1279.
(46) Ghosh, S. Cisplatin: The First Metal Based Anticancer Drug. *Bioorg Chem.* **2019**, *88*, 102925.
(47) Zhou, J.; Kang, Y.; Chen, L.; Wang, H.; Liu, J.; Zeng, S.; Yu, L. The Drug-Resistance Mechanisms of Five Platinum-Based Antitumor Agents. *Front. Pharmacol.* **2020**, *11*, 343.

https://doi.org/10.1021/jacs.2c09820
J. Am. Chem. Soc. 2023, 145, 234−246

(48) Abdalbari, F. H.; Telleria, C. M. The Gold Complex Auranofin: New Perspectives for Cancer Therapy. *Discover Oncol.* **2021**, *12* (1), 1−18.
(49) Marzano, C.; Gandin, V.; Folda, A.; Scutari, G.; Bindoli, A.; Rigobello, M. P. Inhibition of Thioredoxin Reductase by Auranofin Induces Apoptosis in Cisplatin-Resistant Human Ovarian Cancer Cells. *Free Radical Biol. Med.* **2007**, *42* (6), 872−881.
(50) Mészáros, J. P.; Pape, V. F. S.; Szakács, G.; Németi, G.; Dénes, M.; Holczbauer, T.; May, N. V.; Enyedy, É. A. Half-Sandwich Organometallic Ru and Rh Complexes of (N,N) Donor Compounds: Effect of Ligand Methylation on Solution Speciation and Anticancer Activity. *Dalton Trans.* **2021**, *50* (23), 8218−8231.
(51) Thota, S.; Rodrigues, D. A.; Crans, D. C.; Barreiro, E. J. Ru(II) Compounds: Next-Generation Anticancer Metallotherapeutics? *J. Med. Chem.* **2018**, *61* (14), 5805−5821.
(52) Amarsy, I.; Papot, S.; Gasser, G. Stimuli-Responsive Metal Complexes for Biomedical Applications. *Angew. Chem., Int. Ed.* **2022**, *61* (40), e202205900.
(53) Monro, S.; Colón, K. L.; Yin, H.; Roque, J.; Konda, P.; Gujar, S.; Thummel, R. P.; Lilge, L.; Cameron, C. G.; McFarland, S. A. Transition Metal Complexes and Photodynamic Therapy from a Tumor-Centered Approach: Challenges, Opportunities, and Highlights from the Development of TLD1433. *Chem. Rev.* **2019**, *119* (2), 797−828.
(54) Neuditschko, B.; Legin, A. A.; Baier, D.; Schintlmeister, A.; Reipert, S.; Wagner, M.; Keppler, B. K.; Berger, W.; Meier-Menches, S. M.; Gerner, C. Interaction with Ribosomal Proteins Accompanies Stress Induction of the Anticancer Metallodrug BOLD-100/KP1339 in the Endoplasmic Reticulum. *Angew. Chem., Int. Ed.* **2021**, *60* (10), 5063−5068.
(55) Intravesical Photodynamic Therapy (PDT) in BCG Refractory/Intolerant Non-Muscle Invasive Bladder Cancer (NMIBC) Patients. https://clinicaltrials.gov/ct2/show/NCT03945162 (accessed on June 20, 2022).
(56) BOLD-100 in Combination With FOLFOX for the Treatment of Advanced Solid Tumours. https://clinicaltrials.gov/ct2/show/NCT04421820 (accessed on June 19, 2022).
(57) Zou, T.; Lum, C. T.; Lok, C. N.; Zhang, J. J.; Che, C. M. Chemical Biology of Anticancer Gold(III) and Gold(I) Complexes. *Chem. Soc. Rev.* **2015**, *44* (24), 8786−8801.
(58) Lu, Y.; Ma, X.; Chang, X.; Liang, Z.; Lv, L.; Shan, M.; Lu, Q.; Wen, Z.; Gust, R.; Liu, W. Recent Development of Gold(I) and Gold(III) Complexes as Therapeutic Agents for Cancer Diseases. *Chem. Soc. Rev.* **2022**, *51*, 5518−5556.
(59) Mora, M.; Gimeno, M. C.; Visbal, R. Recent Advances in Gold−NHC Complexes with Biological Properties. *Chem. Soc. Rev.* **2019**, *48* (2), 447−462.
(60) Liu, W.; Gust, R. Metal N-Heterocyclic Carbene Complexes as Potential Antitumor Metallodrugs. *Chem. Soc. Rev.* **2013**, *42* (2), 755−773.
(61) Walther, W.; Dada, O.; O'Beirne, C.; Ott, I.; Sánchez-Sanz, G.; Schmidt, C.; Werner, C.; Zhu, X.; Tacke, M. In Vitro and In Vivo Investigations into the Carbene Gold Chloride and Thioglucoside Anticancer Drug Candidates NHC-AuCl and NHC-AuSR. *Lett. Drug Des Discov* **2016**, *14* (2), 125−134.
(62) Elie, B. T.; Hubbard, K.; Pechenyy, Y.; Layek, B.; Prabha, S.; Contel, M. Preclinical Evaluation of an Unconventional Ruthenium-gold-based Chemotherapeutic: RANCE-1, in Clear Cell Renal Cell Carcinoma. *Cancer Med.* **2019**, *8* (9), 4304−4314.
(63) Tialiou, A.; Chin, J.; Keppler, B. K.; Reithofer, M. R. Current Developments of N-Heterocyclic Carbene Au(I)/Au(III) Complexes toward Cancer Treatment. *Biomedicines* **2022**, *10* (6), 1417.
(64) Poursharifi, M.; Wlodarczyk, M. T.; Mieszawska, A. J. Nano-Based Systems and Biomacromolecules as Carriers for Metallodrugs in Anticancer Therapy. *Inorganics* **2019**, *7* (1), 2.
(65) Reches, M.; Gazit, E. Casting Metal Nanowires within Discrete Self-Assembled Peptide Nanotubes. *Science (1979)* **2003**, *300* (5619), 625−627.
(66) Gazit, E. Self-Assembled Peptide Nanostructures: The Design of Molecular Building Blocks and Their Technological Utilization. *Chem. Soc. Rev.* **2007**, *36* (8), 1263−1269.
(67) Rawlings, N. D.; Barrett, A. J.; Finn, R. Twenty Years of the MEROPS Database of Proteolytic Enzymes, Their Substrates and Inhibitors. *Nucleic Acids Res.* **2016**, *44* (D1), D343−D350.
(68) Geng, Y.; Dalhaimer, P.; Cai, S.; Tsai, R.; Tewari, M.; Minko, T.; Discher, D. E. Shape Effects of Filaments versus Spherical Particles in Flow and Drug Delivery. *Nat. Nanotechnol* **2007**, *2* (4), 249−255.
(69) Hackenberg, F.; Müller-Bunz, H.; Smith, R.; Streciwilk, W.; Zhu, X.; Tacke, M. Novel Ruthenium(II) and Gold(I) NHC Complexes: Synthesis, Characterization, and Evaluation of Their Anticancer Properties. *Organometallics* **2013**, *32* (19), 5551−5560.
(70) Liu, W.; Bensdorf, K.; Proetto, M.; Abram, U.; Hagenbach, A.; Gust, R. NHC Gold Halide Complexes Derived from 4,5-Diarylimidazoles: Synthesis, Structural Analysis, and Pharmacological Investigations as Potential Antitumor Agents. *J. Med. Chem.* **2011**, *54*, 8605−8615.
(71) Qiao, Z.-k.; Li, Y.-l.; Lu, H.-t.; Wang, K.-l.; Xu, W.-h. Expression of Tissue Levels of Matrix Metalloproteinases and Tissue Inhibitors of Metalloproteinases in Renal Cell Carcinoma. *World J. Surg. Oncol.* **2013**, *11* (1), 1.
(72) Giambernardi, T. A.; Grant, G. M.; Taylor, G. P.; Hay, R. J.; Maher, V. M.; Mccormick, J. J.; Klebe, R. J. Overview of Matrix Metalloproteinase Expression in Cultured Human Cells. *Matrix Biology* **1998**, *16* (8), 483−496.
(73) Visse, R.; Nagase, H. Matrix Metalloproteinases and Tissue Inhibitors of Metalloproteinases: Structure, Function, and Biochemistry. *Circ. Res.* **2003**, *92* (8), 827−839.
(74) Endo, K.; Maehara, Y.; Baba, H.; Yamamoto, M.; Tomisaki, S.; Watanabe, A.; Kakeji, Y.; Sugimachi, K. Elevated Levels of Serum and Plasma Metalloproteinases in Patients with Gastric Cancer. *Anticancer Res.* **1997**, *17* (3C), 2253−2258.
(75) Tutton, M. G.; George, M. L.; Eccles, S. A.; Burton, S.; Swift, R. I.; Abulafi, A. M. Use of Plasma MMP-2 and MMP-9 Levels as a Surrogate for Tumour Expression in Colorectal Cancer Patients. *Int. J. Cancer* **2003**, *107* (4), 541−550.
(76) Collier, I. E.; Legant, W.; Marmer, B.; Lubman, O.; Saffarian, S.; Wakatsuki, T.; Elson, E.; Goldberg, G. I. Diffusion of MMPs on the Surface of Collagen Fibrils: The Mobile Cell Surface − Collagen Substratum Interface. *PLoS One* **2011**, *6* (9), No. e24029.
(77) Reid, K. B. M. A Collagen-like Amino Acid Sequence in a Polypeptide Chain of Human C1q (a Subcomponent of the First Component of Complement). *Biochem. J.* **1974**, *141* (1), 189−203.
(78) Farina, A. R.; Cappabianca, L.; Desantis, G.; Ianni, N. D.; Ruggeri, P.; Ragone, M.; Merolle, S.; Tonissen, K. F.; Gulino, A.; MacKay, A. R. Thioredoxin Stimulates MMP-9 Expression, de-Regulates the MMP-9/TIMP-1 Equilibrium and Promotes MMP-9 Dependent Invasion in Human MDA-MB-231 Breast Cancer Cells. *FEBS Lett.* **2011**, *585* (20), 3328−3336.
(79) van der Velden, V. H. J.; Hulsmann, A. R. Peptidases: Structure, Function and Modulation of Peptide-mediated Effects in the Human Lung. *Clin. Exp. Allergy* **1999**, *29* (4), 445−456.
(80) Yoshimoto, T.; Orawski, A. T.; Simmons, W. H. Substrate Specificity of Aminopeptidase P from Escherichia Coli: Comparison with Membrane-Bound Forms from Rat and Bovine Lung. *Arch. Biochem. Biophys.* **1994**, *311* (1), 28−34.
(81) Abbott, C. A.; McCaughan, G. W.; Baker, E.; Sutherland, G. R. Genomic Organization, Exact Localization, and Tissue Expression of the Human CD26 (Dipeptidyl Peptidase IV) Gene. *Immunogenetics* **1994**, *40* (5), 331−338.
(82) Fukasawa, K. M.; Fukasawa, K.; Sahara, N.; Harada, M.; Kondo, Y.; Nagatsu, I. Immunohistochemical Localization of Dipeptidyl Aminopeptidase IV in Rat Kidney, Liver, and Salivary Glands. *J. Histochem. Cytochem. Cytochem.* **1981**, *29* (3), 337−343.
(83) Lambeir, A. M.; Durinx, C.; Scharpé, S.; de Meester, I. Dipeptidyl-Peptidase IV from Bench to Bedside: An Update on Structural Properties, Functions, and Clinical Aspects of the Enzyme DPP IV. *Crit Rev. Clin Lab Sci.* **2003**, *40* (3), 209−294.

(84) Schmidt, C.; Albrecht, L.; Balasupramaniam, S.; Misgeld, R.; Karge, B.; Brönstrup, M.; Prokop, A.; Baumann, K.; Reichl, S.; Ott, I. A Gold(i) Biscarbene Complex with Improved Activity as a TrxR Inhibitor and Cytotoxic Drug: Comparative Studies with Different Gold Metallodrugs. *Metallomics* **2019**, *11* (3), 533−545.
(85) Bindoli, A.; Rigobello, M. P.; Scutari, G.; Gabbiani, C.; Casini, A.; Messori, L. Thioredoxin Reductase: A Target for Gold Compounds Acting as Potential Anticancer Drugs. *Coord. Chem. Rev.* **2009**, *253* (11−12), 1692−1707.
(86) Köster, S. D.; Alborzinia, H.; Can, S.; Kitanovic, I.; Wölfl, S.; Rubbiani, R.; Ott, I.; Riesterer, P.; Prokop, A.; Merz, K.; Metzler-Nolte, N. A Spontaneous Gold(I)-Azide Alkyne Cycloaddition Reaction Yields Gold-Peptide Bioconjugates Which Overcome Cisplatin Resistance in a P53-Mutant Cancer Cell Line. *Chem. Sci.* **2012**, *3* (6), 2062−2072.
(87) Śmiłowicz, D.; Slootweg, J. C.; Metzler-Nolte, N. Bioconjugation of Cyclometalated Gold(III) Lipoic Acid Fragments to Linear and Cyclic Breast Cancer Targeting Peptides. *Mol. Pharmaceutics* **2019**, *16* (11), 4572−4581.
(88) Meier-Menches, S. M.; Casini, A. Design Strategies and Medicinal Applications of Metal-Peptidic Bioconjugates. *Bioconjug Chem.* **2020**, *31* (5), 1279−1288.
(89) Monticelli, L.; Kandasamy, S. K.; Periole, X.; Larson, R. G.; Tieleman, D. P.; Marrink, S.-J. The MARTINI Coarse-Grained Force Field: Extension to Proteins. *J. Chem. Theory Comput* **2008**, *4* (5), 819−834.
(90) Marrink, S. J.; Risselada, H. J.; Yefimov, S.; Tieleman, D. P.; de Vries, A. H. The MARTINI Force Field: Coarse Grained Model for Biomolecular Simulations. *J. Phys. Chem. B* **2007**, *111* (27), 7812−7824.
(91) Abraham, M. J.; Murtola, T.; Schulz, R.; Pall, S.; Smith, J. C.; Hess, B.; Lindahl, E. GROMACS: High Performance Molecular Simulations through Multi-Level Parallelism from Laptops to Supercomputers. *SoftwareX* **2015**, *1−2*, 19−25.
(92) Bussi, G.; Donadio, D.; Parrinello, M. Canonical Sampling through Velocity Rescaling. *J. Chem. Phys.* **2007**, *126* (1), No. 014101.
(93) Hess, B. P-LINCS: A Parallel Linear Constraint Solver for Molecular Simulation. *J. Chem. Theory Comput* **2008**, *4* (1), 116−122.
(94) Eisenhaber, F.; Lijnzaad, P.; Argos, P.; Sander, C.; Scharf, M. The Double Cubic Lattice Method: Efficient Approaches to Numerical Integration of Surface Area and Volume and to Dot Surface Contouring of Molecular Assemblies. *J. Comput. Chem.* **1995**, *16* (3), 273−284.
(95) Humphrey, W.; Dalke, A.; Schulten, K. VMD: Visual Molecular Dynamics. *J. Mol. Graph.* **1996**, *14* (1), 33−38.

https://doi.org/10.1021/jacs.2c09820
J. Am. Chem. Soc. 2023, 145, 234−246